Synthesis of bismuth oxybromochloroiodide/graphitic carbon nitride quaternary composites ($BiO_xCl_y/BiO_mBr_n/BiO_pI_q$/g-$C_3N_4$) enhances visible-light-driven photocatalytic activity

Yu-Yun Lin, Jiun-Ting Hung, Yu-Chen Chou, Shi-Jie Shen, Wu-Tsan Wu, Fu-Yu Liu, Jia-Hao Lin, Chiing-Chang Chen [*]

Department of Science Education and Application, National Taichung University of Education, 403 Taichung, Taiwan

ARTICLE INFO

ABSTRACT

$BiO_xCl_y/BiO_mBr_n/BiO_pI_q$/g-$C_3N_4$ was prepared by using the hydrothermal synthesis. The composition and morphologies of the composites were controlled by adjusting the reaction pH value, temperature, and molar ratio. The optimized $BiO_xCl_y/BiO_mBr_n/BiO_pI_q$/g-$C_3N_4$ photocatalyst increased the rate of photocatalytic conversion from CO_2 to CH_4 to 0.036 µmol g^{-1} h^{-1} and these samples were subjected to photocatalytic degradation with CV. The enhanced photocatalytic activity can be attributed to the effective separation of photogenerated carriers driven by the photoinduced potential difference generated at these heterostructure interfaces, the transfer of photogenerated electrons through the g-C_3N_4 skeleton, and the favorable alignment of the straddling band structure from $BiO_xCl_y/BiO_mBr_n/BiO_pI_q$/g-$C_3N_4$.

1. Introduction

BiOX photocatalysts have previously been employed in applications such as water splitting [1], carbon dioxide photoreduction [2], nitrogen fixation [3], solar cells [4], bacterial disinfection [5], air pollutant removal [6], heavy metal oxidation [7], and photodynamic therapy [8]. This paper focuses on carbon dioxide photoreduction and photocatalytically remediating persistent organic pollutants. The layered structure of bismuth oxyhalide results in the favorable separation efficiency of photogenerated electron–hole pairs, which, as confirmed by scores of scholars, can prompt photocatalytic degradation, thereby improving photocatalytic activity.

In 1979, a study presented the photocatalytic conversion of CO_2 to HCOOH and CH_3OH through the use of semiconductor powders in water [9]. In the past few years, scientists have been committed to the development of new photocatalysts, including those belonging to the BiOX family [2,10]. In one study, photoinduced oxygen vacancies were easily formed on the BiOX surface; this is extremely beneficial to the activation of highly inert CO_2 molecules [11]. Although numerous reports have been published on the use of BiOX photocatalysts for CO_2 reduction, the efficiency of this process remains extremely low. To enable BiOX to improve the efficiency and selectivity of CO_2 conversion, the function and type of defects must be delineated.

Triphenylmethane dyes, such as crystal violet (CV), are widely used because they are cheap and easily available. In numerous countries and regions, such dyes are banned chemicals. If wastewater from dyeing and finishing is discharged into rivers at will, environmental disasters may occur, causing mucosal ulcers, gastroenteritis, nausea, and other human health problems [12]. To protect the environment and prevent such problems, such wastewater must be properly treated. Multiple methods for degrading organic pollutants have been developed, including chemical oxidation [13], absorption [14], electrochemical condensation [15] and biodegradation [16], and photocatalysis [17]. The reaction process of each method has its own limitations or drawbacks. Chemical oxidation cannot mineralize all organic matter, and pollutants cannot be degraded through absorption. Electrochemical condensation produces a large amount of sludge, and biodegradation both consumes large amounts of oxygen and requires long reaction times. Photocatalysis, which is characterized by the rapid degradation and mineralization of pollutants, is more favorable. Given that this method can be used to treat wastewater, remediate the environment, and decompose water to produce hydrogen and oxygen, it has attracted a considerable amount of scholarly attention such that numerous related studies have been conducted in recent years.

Here, quaternary $BiO_xCl_y/BiO_mBr_n/BiO_pI_q/g\text{-}C_3N_4$ was prepared through one-step controlled hydrothermal synthesis and a template-free method. This series is highly promising because of its excellent controllability, conductivity, transparency, and adsorption. We applied this catalyst to CO_2 reduction and CH_4 generation and in the photo-degradation of CV, these quaternary complexes have higher removal rates than BiO_xCl_y BiO_mBr_n/BiO_pI_q. The study of reaction pathways driven by visible light extends the understanding of organic compound degradation and environmental remediation.

2. Experimental

2.1. Synthesis of $BiO_xCl_y/BiO_mBr_n/BiO_pI_q/g\text{-}C_3N_4$

A series of $BiO_xCl_y/BiO_mI_n/BiO_pI_q$ composite materials were prepared under controlled pH and temperature conditions. Identifiers ranging from BC1B1I1–1-100 to BC1B1I1–13-250, take BC1B1I1–1-100 as an example, B means $(Bi(NO_3)_3 \cdot 5H_2O)$, C1B1I1 means [KCl]: [KBr]: [KI] = 1:1:1, 1 means pH = 1, 100 represents the reaction temperature, are used herein to denote the samples synthesized [18], as shown in Table S1.

This process entailed first mixing 500–x mg of BC1B1I1–10-100 and x mg of g-C_3N_4 in a flask (15 mL) at varying amounts (10, 25, 50, 75, and 90 wt%) and then introducing 10 mL of ethylene glycol. The derived substrate was stirred for a 30-min period, after which it was transferred to a polytetrafluoroethylene-lined autoclave that was subsequently heated to and then maintained at 100 °C for 4 h. The derived solid

precipitate was filtered, and any ionic species was removed by washing with a deionized water and ethanol. Subsequently, the precipitate was dried for 12 h at 60 °C. We used identifiers ranging from BC1B1I1–10–100-10 wt% C3N4 to BC1B1I1–10–100-90 wt% C3N4 to label the samples (Table S2).

2.2. Photocatalysis experiments

2.2.1. Photocatalytic reduction of CO_2

CO_2 was photocatalytically reduced over several hours under a pressure of 2 bar. Degassing by helium purging was performed to check the quartz reactor for leaks. CO_2 of high purity (99.99%) was placed into the reactor at a 500 mL/min delivery rate by using the mass flow controller. We executed a CO_2 saturation process in a photoreactor containing an aqueous solution (1 N) of NaOH and a photocatalyst (0.2 g) for photoreduction. For product analysis, a syringe was used to extract from the photoreactor a sample that was then placed on the gas chromatography column.

2.2.2. Photocatalytic degradation of CV

We prepared a Pyrex glass vessel containing 100 mL of a 100-ppm aqueous solution of CV and 50 mg of photocatalyst for the photocatalysis experiments. Before irradiation, the suspension was mixed with a magnetic stirrer in darkness for 30 min to achieve the adsorption–desorption equilibrium between the catalyst surface and CV. Next, a 5-mL aliquot was collected, and through centrifugation, the catalyst was removed. For the remaining dye in each reaction cycle, the
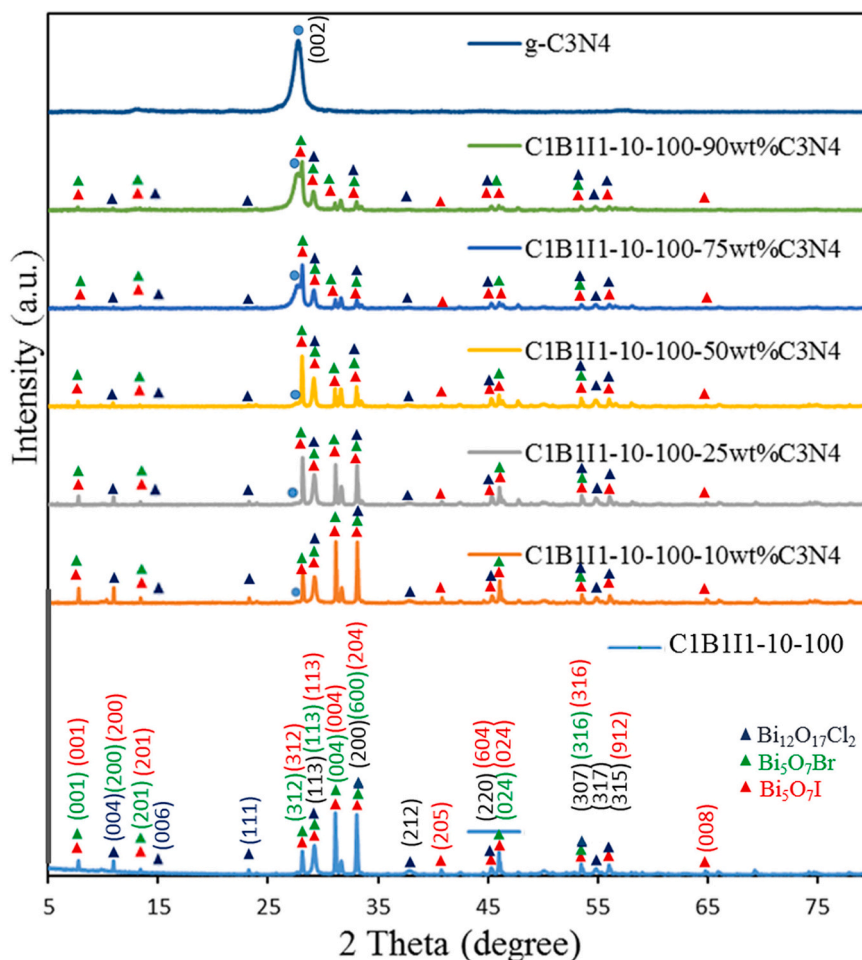

Fig. 1. XRD patterns of as-prepared $Bi_{12}O_{17}Cl_2/Bi_5O_7Br/ Bi_5O_7I$ meterials obtained by using different content of g-C_3N_4. (reaction temperature = 100 °C, pH value =10, reaction time = 12 h).

concentration was quantified through UV–Vis spectrophotometry.

3. Results and discussion

3.1. $BiO_xCl_y/BiO_mBr_n/BiO_pI_q/g\text{-}C_3N_4$ composite characterization

The fingerprints of 10 composites, namely BiOCl, Bi_3O_4Cl, $Bi_{12}O_{17}Cl_2$, BiOBr, Bi_4O_5Br, Bi_3O_4Br, Bi_5O_7Br, $Bi_{24}O_{31}Br_{10}$, BiOI, and Bi_5O_7I, without the addition of $g\text{-}C_3N_4$ were prepared, are presented in Figs. S1-S4 and Table S3 [19]. As shown in Fig. 1, the $Bi_{12}O_{17}Cl_2/$ $Bi_5O_7Br/Bi_5O_7I/g\text{-}C_3N_4$ composite was present. From JCPDS data, $Bi_{12}O_7C_{l2}$ (JCPDS 37–0702) crystallizes in the tetragonal type crystal structure, Bi_5O_7Br (JCPDS 38–0493) and Bi_5O_7I (JCPDS 40–0548) crystallize in the orthorhombic structure type structure. Changes in the content of $g\text{-}C_3N_4$, as determined through XRD. This as-prepared sample contained phases of $Bi_{12}O_{17}Cl_2$, Bi_5O_7Br, Bi_5O_7I, and $g\text{-}C_3N_4$ that were derived under a pH, reaction temperature, and KCl:KBr:KI molar ratio of 10, 100 °C, and 1:1:1, respectively.

The transmission electron microscope (TEM) images (Fig. 2) revealed that $Bi_{12}O_{17}Cl_2/Bi_5O_7Br/Bi_5O_7I/g\text{-}C_3N_4$ was composed of thin flakes of varying sizes. The EDS spectra demonstrated that these flakes contained carbon, nitrogen, oxygen, chlorine, bromine, iodine, and bismuth. From the XRD patterns, we calculated the lattice spacing for the (1 1 7) plane of $Bi_{12}O_{17}Cl_2$, (3 1 2) plane of Bi_5O_7Br, and (0 2 4) plane of Bi_5O_7I. We determined three sets of lattice images, which we found to correspond to d-spacings of 0.306, 0.315, and 0.196 nm (Fig. 2B). Under

different pH values, the following changes were observed: BiO-Cl→$Bi_4O_5Cl_2$ → $Bi_{24}O_{31}Cl_{10}$ → Bi_3O_4Cl → $Bi_{12}O_{17}Cl_2$, BiOBr→$Bi_4O_5Br_2$ → Bi_3O_4Br → Bi_5O_7Br → $Bi_{12}O_{17}Br_2$, and BiOI→$Bi_4O_5I_2$ → $Bi_7O_9I_3$ → Bi_3O_4I → Bi_5O_7I [18].

Field emission scanning electron microscope (FESEM) images of $Bi_{12}O_{17}Cl_2/Bi_5O_7Br/Bi_5O_7I$ and $Bi_{12}O_{17}Cl_2/Bi_5O_7Br/Bi_5O_7I/10wt\%g\text{-}C_3N_4$ (Fig. S5) revealed large-grain crystals, irregular ultraflakes, ultraflakes, and ultrathin irregular flaky crystals. The halogen atoms in the layers were strongly covalently bonded. The weak forces between the layers are likely van der Waals forces. In general, a crystal structure characterized by open layers provides sufficient space for forming an inherent internal electrostatic field along the crystal orientation perpendicular to the $[Bi_2O_2]$ and [X] slices. This is accomplished through the polarization of related atoms and orbitals [20]. This electrostatic field can induce photogenerated electron–hole pairs to separate—the key to the excellent photocatalytic activity of the BiOX family [21].

The FTIR results of the $Bi_{12}O_{17}Cl_2/Bi_5O_7Br/Bi_5O_7I/g\text{-}C_3N_4$ composites (Fig. S6). We identified peaks at 1569, 1409, 1319, and 1241 cm^{-1} and ascribed them to aromatic C-N stretching [22]. Our results also indicated a band appearing at 813 cm^{-1}, which we ascribed to out-of-plane bending modes of C-N heterocyclic compounds [23].

The chemical compositions of the $Bi_{12}O_{17}Cl_2/Bi_5O_7Br/Bi_5O_7I/g\text{-}C_3N_4$ samples were investigated through High-resolution X-ray photoelectron spectroscopy (HR-XPS). $Bi_{12}O_{17}Cl_2/Bi_5O_7Br/Bi_5O_7I/g\text{-}C_3N_4$ photocatalysts were composed of N 1 s, C 1 s, O 1 s, I 3d, Br 3d, Cl 2p, and

Element	Weight%	Atomic%
C K	18.33	47.87
N K	15.27	34.21
O K	3.47	6.80
Cl K	0.69	0.61
Br K	2.17	0.85
I L	6.61	1.63
Bi L	53.47	8.03
Totals	100.00	
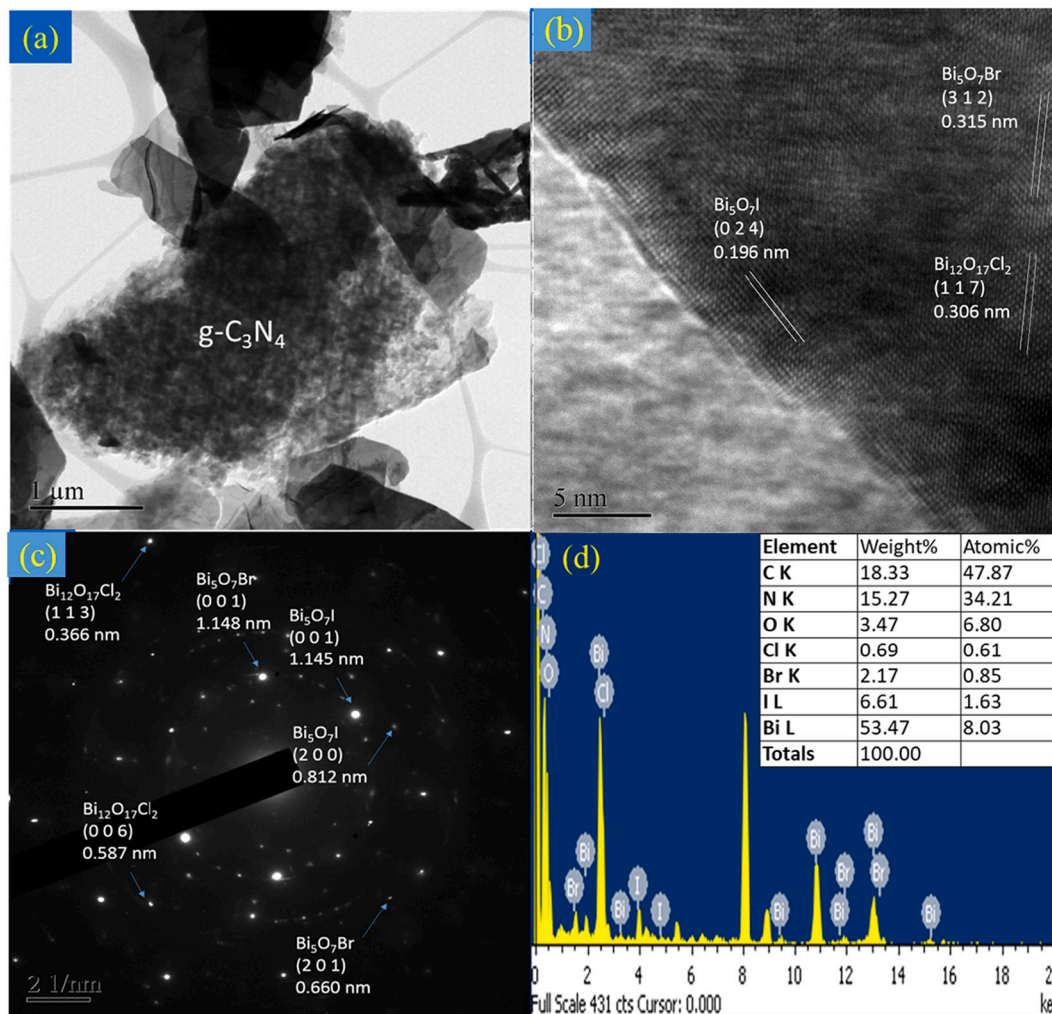
Fig. 2. FE-TEM images and EDS of $Bi_{12}O_{17}Cl_2/Bi_5O_7Br/$ $Bi_5O_7I/g\text{-}C_3N_4$.

Bi 4f (Fig. S7A–G).

C 1 s spectra (Fig. S7F) mainly demonstrated sp^2 C − C bonds (283.2 eV) and sp^2-hybridized carbon as two carbon species existing in the N-containing aromatic ring N (N − C=N; 286.9 eV). As indicated in Fig. S7G, the peak of the N1 s spectrum at 397.6 eV and the peak at 399.0 eV corresponded to the sp^2 hybrid N within the triazine ring (C−N=C) and the tertiary N−(C)₃ group, respectively. These two units made up the fundamental substructural units of heptazine heterocyclic rings in g-C₃N₄ polymers, in addition to sp^2-hybridized carbon (N − C=N, 286.9 eV).

Diffuse reflectance spectroscopy (DRS) data of $Bi_{12}O_{17}Cl_2$/Bi_5O_7Br/Bi_5O_7I samples containing varying percentages of g-C₃N₄. As the percentage of g-C₃N₄ increased, the sample's absorption edge regularly shifted to a longer wavelength region. The photographs in the chart at the top of Fig. S8 depict the gradual color changes in the $Bi_{12}O_{17}Cl_2$/Bi_5O_7Br/Bi_5O_7I/g-C₃N₄ samples. As the proportion of added g-C₃N₄ increased, the color grew increasingly lighter, with the pure g-C₃N₄ appearing light yellow. By using the formula $E_g = 1240/\lambda$ (eV), where λ is the wavelength (nm) corresponding to the intersection point of the horizontal and vertical parts of the spectrum [24], we derived the

sample's band gap energy E_g from the absorption data. The wavelength range was between 420 and 550 nm, and the E_g value was between 2.25 and 2.95 eV. The literature indicates that the E_g values of pure $Bi_{12}O_{17}Cl_2$, Bi_5O_7Br, and Bi_5O_7I are nearly 2.19 [25], 2.80 [26], and 2.92 eV [27], respectively.

For $Bi_{12}O_{17}Cl_2$/Bi_5O_7Br/Bi_5O_7I and $Bi_{12}O_{17}Cl_2$/Bi_5O_7Br/Bi_5O_7I/g-C₃N₄, the curves illustrating the adsorption–desorption isotherms measured with nitrogen gas are presented in Fig. S9. On the basis of the International Union of Pure and Applied Chemistry classification and under the Brunauer-Emmett-Teller (BET) method, five adsorption isotherms constitute Type IV isotherms with H3 hysteresis loops. We determined S_{BET} values of 9.3795 and 10.2586 m²/g, pore volumes of 0.075604 and 0.084904 cm³/g, and diameters of 492.115 and 368.588 nm for the $Bi_{12}O_{17}Cl_2$/Bi_5O_7Br/Bi_5O_7I and $Bi_{12}O_{17}Cl_2$/Bi_5O_7Br/Bi_5O_7I/g-C₃N₄ samples, respectively. An abundance of active sites on the surface explained the high S_{BET} and pore volume; they are conducive to the transport of reactants, thereby promoting increases in photocatalytic efficiency. The high S_{BET} and pore volume of $Bi_{12}O_{17}Cl_2$/Bi_5O_7Br/Bi_5O_7I/g-C₃N₄ may be responsible for its photocatalytic efficiency.
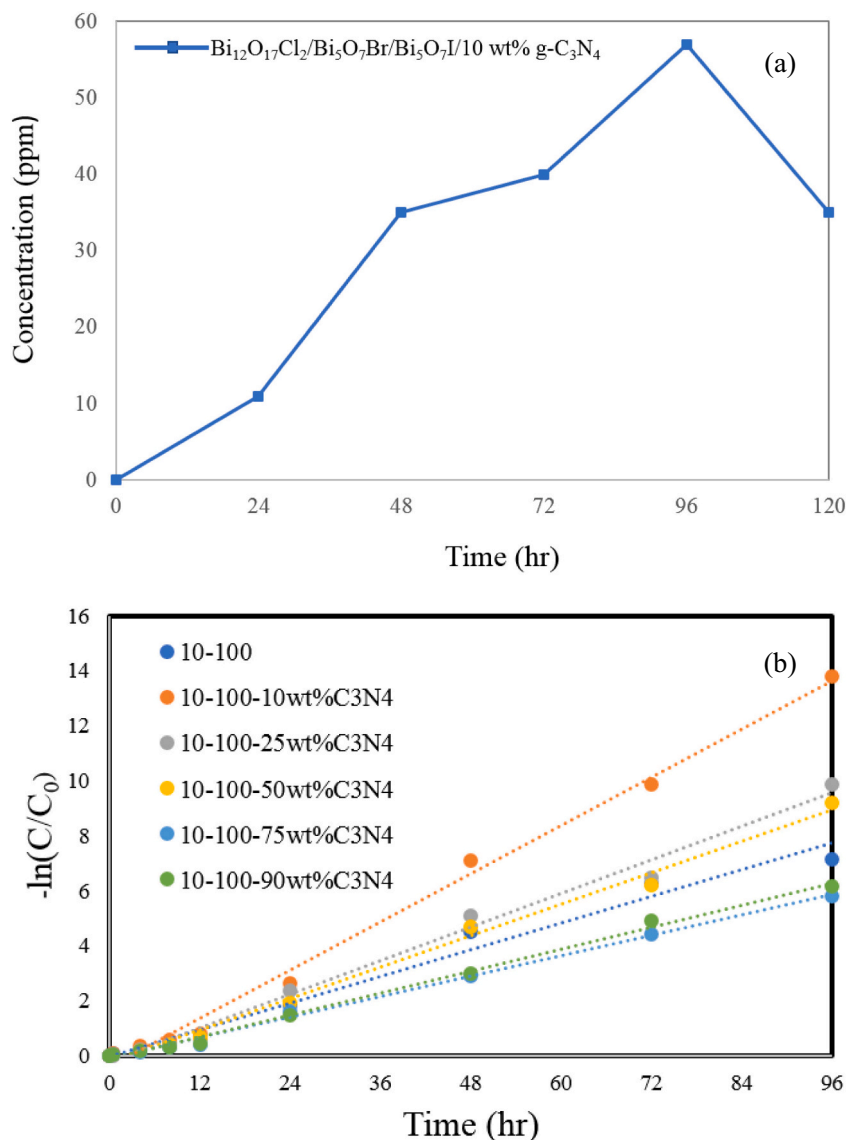
Fig. 3. (a) Photocatalytic reduction of CO₂ as a function of irradiation time over $Bi_{12}O_{17}Cl_2$/Bi_5O_7Br/Bi_5O_7I/10 wt% g-C₃N₄, (b) photocatalytic degradation of CV as a function of visible-light-driven irradiation time over $Bi_{12}O_{17}Cl_2$/Bi_5O_7Br/Bi_5O_7I/g-C₃N₄. (Molar ratio KCl:KBr:KI =1:1:1, hydrothermal conditions: temp = 100 °C, pH = 10, time = 12 h).

3.2. Photocatalytic activity

3.2.1. CO₂ photoreduction performance

Through irradiation at 1 atm and 25 °C, the CO_2–CH_4 conversion efficiency was enhanced to 0.036 µmol g^{-1} h^{-1} by the optimized $Bi_{12}O_{17}Cl_2$/Bi_5O_7Br/Bi_5O_7I/10 wt% g-C_3N_4 (Fig. 3A). From the GC data, except for methane, no other products were found, indicating that the photocatalyst has good selectivity. The results of this study with those in literature are presented in Table S4 [2,28]. Due to differences in reactor systems, or those literature did not report the light intensity entering the reactor or the area of catalyst irradiated, nor do they calculate quantum yield. Although the yields reported by others in terms of µmol $h^{-1}g^{-1}$, the yields reported by others cannot be directly compared [29]. Low performance may occur when measurements are made at low irradiance, which is the main factor controlling yield, so it may be beneficial to provide higher light intensity to $Bi_{12}O_{17}Cl_2$/Bi_5O_7Br/Bi_5O_7I/10 wt% g-C_3N_4 to generate CH_4 product for CO_2 photoreduction.

3.2.2. Photodegradation of CV

Fig. 3B presents the photocatalytic degradation of CV as a function of visible light irradiation time over an $Bi_{12}O_{17}Cl_2$/Bi_5O_7Br/Bi_5O_7I/g-C_3N_4 aqueous solution, as examined on a UV–Vis spectrophotometer. $Bi_{12}O_{17}Cl_2$/Bi_5O_7Br/Bi_5O_7I/10 wt% g-C_3N_4, over 96 h of irradiation, photocatalytically outperformed the other catalysts, and the CV removal efficiency was as high as 99%. To better understand the degradation kinetics, a pseudo-first-order model was experimentally implemented [30]. Specifically, $\ln(C_0/C) = kt$, where k is the first order of the decolorization rate. We determined that the k value of $Bi_{12}O_{17}Cl_2$/Bi_5O_7Br/Bi_5O_7I/10 wt% g-C_3N_4 (BC1B1I1–10–100-10 wt% C3N4) was 1.457×10^{-1} h^{-1} (highest rate of degradation) in Table 1. Of all the samples, the $Bi_{12}O_{17}Cl_2$/Bi_5O_7Br/Bi_5O_7I/10 wt% g-C_3N_4 composite material, with a large S_{BET}, had the most favorable photocatalytic performance. Notably, high reuse potential and chemical stability were identified as characteristics of the $Bi_{12}O_{17}Cl_2$/Bi_5O_7Br/Bi_5O_7I/10 wt% g-C_3N_4 photocatalyst. After the used catalyst was recycled, the catalyst could be obtained by centrifugal separation after each cycle. Over five cycles, the catalyst's performance remained almost stable, with no clear defects in photocatalytic activity (Fig. S10A); the CV degradation rate remained at 73.9%, demonstrating outstanding recyclability. XRD indicated that the fresh and spent photocatalysts did not differ (Fig. S10B).

3.3. Pathways of CO₂ conversion and CV photodegradation

We have observed that under optimal conditions, $Bi_{12}O_{17}Cl_2$/Bi_5O_7Br/Bi_5O_7I/g-C_3N_4 promotes (0.036 µmolg^{-1} h^{-1}) CO_2 photocatalytic conversion to CH_4 at 25 °C and 1 atm pressure, which indicates that $Bi_{12}O_{17}Cl_2$/Bi_5O_7Br/Bi_5O_7I/g-C_3N_4 has a decisive advantage in CH_4 production and has great potential in applications involving CO_2 conversion catalysis. In the presence of $Bi_{12}O_{17}Cl_2$/Bi_5O_7Br/Bi_5O_7I/g-C_3N_4 the removal and conversion efficiency is significantly improved. Fig. 4A shows the CO_2 photocatalytic reduction reaction mechanism of $Bi_{12}O_{17}Cl_2$/Bi_5O_7Br/Bi_5O_7I/g-C_3N_4 photocatalyst. Photochemical

reduction studies of CO_2 (adsorbed in water) indicate that H_2CO_3 and dissolved CO_2 may be active substances [31,32].

We also executed separation distance measurements to study the separation ability of the $Bi_{12}O_{17}Cl_2$/Bi_5O_7Br/Bi_5O_7I/g-C_3N_4 photogenerated carriers (Fig. S11), the photoluminescence (PL) intensity of $Bi_{12}O_{17}Cl_2$/Bi_5O_7Br/Bi_5O_7I/10 wt% g-C_3N_4 was the lowest among those of the prepared materials. This composite is expected to exhibit favorable photocatalytic performance in UV–Vis semiconductor lighting devices because, as confirmed from the PL results, it is essential in hindering electron–hole recombination.

Relevant active reactive oxygen species were eliminated through the use of four quenchers in the testing of photocatalytic activity [33]. Specifically, $^1O_2$, $^\bullet O_2^-$, h$^+$, and $^\bullet OH$ were captured using sodium azide (SA, 1.0 mM), p-Benzoquinone (BQ, 1.0 mM), ammonium oxalate (AO, 1.0 mM), and isopropanol (IPA, 1.0 mM), respectively. The AO and IPA degradation efficiency was not as favorable as that of BQ, as presented in Fig. S12A. SA did not influence photocatalytic CV degradation. The scavenging results demonstrated that $^\bullet O_2^-$ was more active in the CV degradation process than h$^+$ or $^\bullet OH$. Furthermore, the generation of $^\bullet OH$ was caused by the multistep reduction of $^\bullet O_2^-$. The active substance $^\bullet O_2^-$ was the primary active species. The secondary active species were h$^+$ and $^\bullet OH$, and the role of $^1O_2$ was negligible. Conducive to CV decomposition, $^\bullet O_2^-$ was generated using dissolved oxygen to capture photogenerated electrons. Results from the analysis of the energy band structure of $Bi_{12}O_{17}Cl_2$/Bi_5O_7Br/Bi_5O_7I/10 wt% g-C_3N_4 are consistent with our proposed mechanism of photocatalysis and were further verified through the identification of active free radicals by using electron spin resonance (ESR) spin trapping; in this process, 5,5-dimethylpyridine-N-oxide (DMPO) was employed. In the ESR spectra obtained using the $Bi_{12}O_{17}Cl_2$/Bi_5O_7Br/Bi_5O_7I/10 wt% g-C_3N_4/visible light system (Fig. S12B-C), in line with the scavenging results, the presence of $^\bullet OH$ and $^\bullet O_2^-$ species was confirmed by the characteristic signals observed for the spin adducts of DMPO-$^\bullet O_2^-$ and DMPO-$^\bullet OH$ (intensity ratios 1:1:1:1 and 1:2:2:1, respectively) [34]. In sum, ethiofencarb degradation with the proposed photocatalytic system was primarily achieved by $^\bullet O_2^-$ and $^\bullet OH$ radicals, with a partial contribution from the photogenerated holes.

The photocatalytic mechanism of the $Bi_{12}O_{17}Cl_2$/Bi_5O_7Br/Bi_5O_7I/10 wt% g-C_3N_4 system provides insights into dye decolorization applications. Photosensitization proceeded concurrently with photocatalysis (Fig. 4B). Under conditions related to photocatalytic reactions and photosensitization, the generation of oxygen free radicals ($^\bullet O_2^-$) could be ascribed to elements reacting with photosensitized and photogenerated electrons as well as with the oxygen on the photocatalyst surface. Following these reactions, $^\bullet O_2^-$ radical–H$^+$ ion reactions occurred, and $^\bullet OH$ radicals were produced through OH$^-$ trapping by holes (h$^+$).

4. Conclusions

A template-free controlled hydrothermal synthesis of a series of quaternary $Bi_{12}O_{17}Cl_2$/Bi_5O_7Br/Bi_5O_7I/g-C_3N_4 photocatalysts was performed. Various temperature and pH conditions were applied to fine-tune the composition of the composites. The photocatalytic performance of $Bi_{12}O_{17}Cl_2$/Bi_5O_7Br/Bi_5O_7I/g-C_3N_4 was ascribable to heterojunction formation, which overcame the inhibition of photocatalytic efficiency caused by the rapid photogenerated electron–hole recombination. Overall, a low-energy band structure, high BET surface area, heterojunction formation, and the layer structure were responsible for the enhanced performance of $Bi_{12}O_{17}Cl_2$/Bi_5O_7Br/Bi_5O_7I/g-C_3N_4. Under 1 atm of pressure and at 25 °C, $Bi_{12}O_{17}Cl_2$/Bi_5O_7Br/Bi_5O_7I/g-C_3N_4 improved the CO_2–CH_4 photocatalytic conversion rate to 0.036 µmol g^{-1} h^{-1} and $^\bullet O_2^-$ constituted the principal active substance in the CV photodegradation reaction.

Table 1

The rate constants (pseudo-first-order) for the photocatalytic degradation of CV with $Bi_{12}O_{17}Cl_2$/Bi_5O_7Br/ Bi_5O_7I/g-C_3N_4 photocatalysts under visible-light-driven irradiation.

Sample code	k (h^{-1})
BC1B1I1–10–100	0.0808
BC1B1I1–10–100-10%C3N4	0.1457
BC1B1I1–10–100-25%C3N4	0.1015
BC1B1I1–10–100-50%C3N4	0.0954
BC1B1I1–10–100-75%C3N4	0.0619
BC1B1I1–10–100-90%C3N4	0.0666
g-C_3N_4	0.0313

(a)

(b)
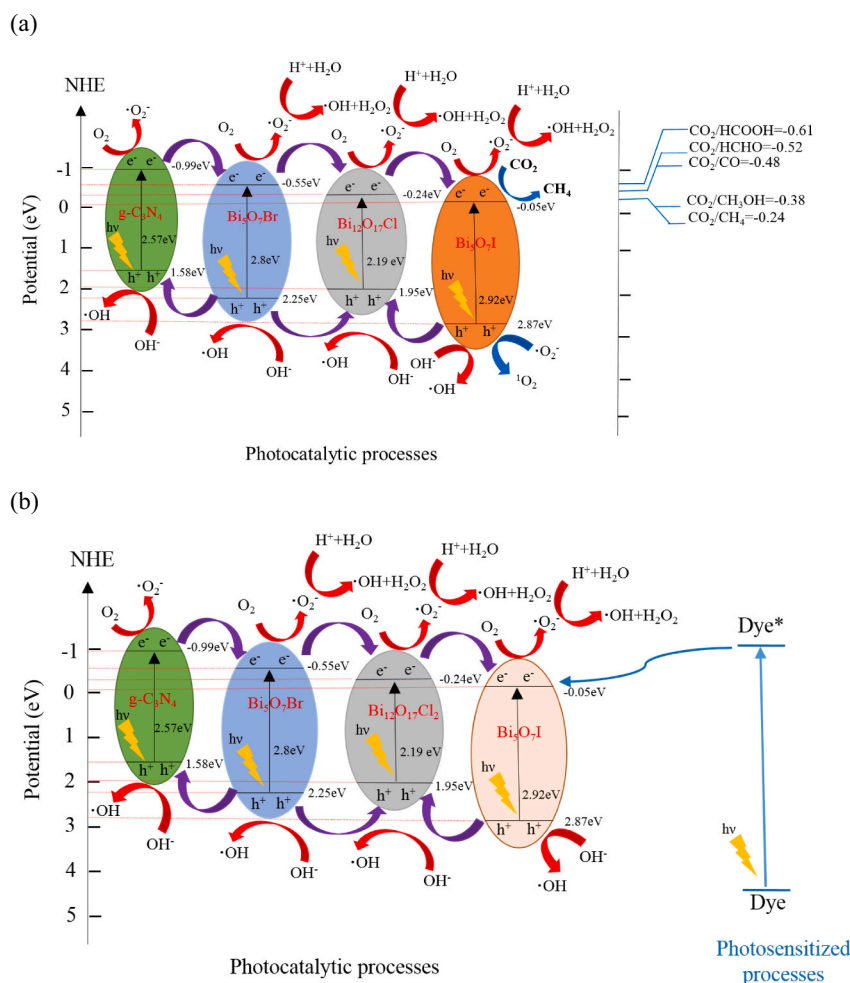
Fig. 4. The band diagram of $Bi_{12}O_{17}Cl_2/Bi_5O_7Br/Bi_5O_7I/g-C_3N_4$ and the probable charge segregation pathways for the (a) photocatalytic reduction of CO_2 and (b) photocatalytic degradation of crystal violet. (For interpretation of the references to color in this figure legend, the reader is referred to the web version of this article.)

CRediT authorship contribution statement

Yu-Yun Lin: Methodology, Data curation, Investigation, Writing – original draft, Software, Writing – review & editing. **Jiun-Ting Hung:** Methodology, Validation, Investigation, Software, Methodology. **Yu-Chen Chou:** Methodology, Software. **Shi-Jie Shen:** Writing – review & editing, Data curation. **Wu-Tsan Wu:** Software, Methodology. **Fu-Yu Liu:** Data curation, Methodology. **Jia-Hao Lin:** Methodology, Data curation. **Chiing-Chang Chen:** Supervision, Conceptualization, Visualization, Writing – review & editing, Validation, Software.

Declaration of Competing Interest

The authors declare that they have no known competing financial interests or personal relationships that could have appeared to influence the work reported in this paper.

Appendix A. Supplementary data

Supplementary data to this article can be found online at https://doi.org/10.1016/j.catcom.2022.106418.

References

[1] G. Lee, Y. Zheng, J. Wu, J., Fabrication of hierarchical bismuth oxyhalides (BiOX, X = Cl, Br, I) materials and application of photocatalytic hydrogen production from water splitting, Catal. Today 307 (2018) 197–204, https://doi.org/10.1016/j.cattod.2017.04.044.

[2] X. Ren, M. Gao, Y. Zhang, Z. Zhang, X. Cao, B. Wang, X. Wang, Photocatalytic reduction of CO_2 on BiOX: effect of halogen element type and surface oxygen vacancy mediated mechanism, Appl. Catal. B Environ. 274 (2020), 119063, https://doi.org/10.1016/j.apcatb.2020.119063.

[3] P. Li, S. Gao, Q. Liu, P. Ding, Y. Wu, C. Wang, S. Yu, W. Liu, Q. Wang, S. Chen, Recent progress of the design and engineering of bismuth oxyhalides for photocatalytic nitrogen fixation, Adv. Energy Sustain. Res. 2 (2021) 2000097, https://doi.org/10.1002/aesr.202000097.

[4] S. Sfaelou, D. Raptis, V. Dracopoulos, P. Lianos, BiOI solar cells, RSC Adv. 5 (2015) 95813–95816, https://doi.org/10.1039/C5RA19835F.

[5] J. Liang, F. Liu, M. Li, W. Liu, M. Tong, Facile synthesis of magnetic Fe_3O_4@BiOI@ AgI for water decontamination with visible light irradiation: different mechanisms for different organic pollutants degradation and bacterial disinfection, Water Res. 137 (2018) 120–129, https://doi.org/10.1016/j.watres.2018.03.027.

[6] X. Hu, C. Li, Z. Sun, J. Song, S. Zheng, Enhanced photocatalytic removal of indoor formaldehyde by ternary heterogeneous $BiOCl/TiO_2$/sepiolite composite under solar and visible light, Build. Environ. 168 (2020), 106481, https://doi.org/10.1016/j.buildenv.2019.106481.

[7] X. Sun, J. Lu, J. Wu, D. Guan, Q. Liu, N. Yan, Enhancing photocatalytic activity on gas-phase heavy metal oxidation with self-assembled BiOI/BiOCl microflowers, J. Colloid Interface Sci. 546 (2019) 32–42, https://doi.org/10.1016/j.jcis.2019.03.049.

[8] L. Xu, F. He, C. Wang, S. Gai, A. Gulzar, D. Yang, C. Zhong, P. Yang, Lanthanide-doped bismuth oxobromide nanosheets for self-activated photodynamic therapy, J. Mater. Chem. B 5 (2017) 7939–7948, https://doi.org/10.1039/C7TB01983A.

[9] T. Inoue, A. Fujishima, S. Konishi, K. Honda, Photoelectrocatalytic reduction of carbon dioxide in aqueous suspensions of semiconductor powders, Nature 277 (1979) 637–638, https://doi.org/10.1038/277637a0.

[10] P. Liu, H. Liu, S. Zhang, J. Wang, C. Wang, A general strategy for obtaining BiOX nanoplates derived Bi nanosheets as efficient CO_2 reduction catalysts by enhancing $CO_2^{\bullet-}$ adsorption and electron transfer, J. Colloid Interface Sci. 602 (2021) 740–747, https://doi.org/10.1016/j.jcis.2021.06.010.

[11] X. Ren, M. Gao, Y. Zhang, Z. Zhang, X. Cao, B. Wang, X. Wang, Photocatalytic reduction of CO_2 on BiOX:Effect of halogen element type and surface oxygen vacancy mediated mechanism, Appl. Catal. B Environ. 274 (2020), 119063, https://doi.org/10.1016/j.apcatb.2020.119063.

[12] D. Vitale, M.M. Suárez-Varela, Y. Picó, Wastewater-based epidemiology, a tool to bridge biomarkers of exposure, contaminants, and human health, Curr. Opin. Environ. Sustain. 20 (2021), 100229, https://doi.org/10.1016/j.coesh.2021.100229.

[13] J. Ma, Y. Ma, X. Rong, Q. Song, B. Wu, X. Lan, Y. Feng, X. Qiu, P. Zhang, Persulfate-based controlled release beads for in situ chemical oxidation of common organic pollutants, J. Environ. Chem. Eng. 9 (2021), 105627, https://doi.org/10.1016/j.jece.2021.105627.

[14] M.A. Nejad, C. Mücksch, H.M. Urbassek, Insulin adsorption on crystalline SiO_2: comparison between polar and nonpolar surfaces using accelerated molecular-dynamics simulations, Chem. Phys. Lett. 670 (2017) 77–83, https://doi.org/10.1016/j.cplett.2017.01.002.

[15] A.S. Naje, S. Chelliapan, Z. Zakaria, S.A. Abbs, Electrocoagulation using a rotated anode: a novel reactor design for textile wastewater treatment, J. Environ. Manag. 176 (2016) 34–44, https://doi.org/10.1016/j.jenvman.2016.03.034.

[16] P. Kumari, Y. Kumar, Chapter 19 - Bioinformatics and computational tools in bioremediation and biodegradation of environmental pollutants, in: Bioremediation for Environmental Sustainability: Approaches to Tackle Pollution for Cleaner and Greener Society, 2021, pp. 421–444, https://doi.org/10.1016/B978-0-12-820318-7.00019-8.

[17] Z. Wang, L. Jiang, K. Wang, Y. Li, G. Zhang, Novel AgI/BiSbO₄ heterojunction for efficient photocatalytic degradation of organic pollutants under visible light: interfacial electron transfer pathway, DFT calculation and degradation mechanism study, J. Hazard. Mater. 410 (2021), 124948, https://doi.org/10.1016/j.jhazmat.2020.124948.

[18] C. Siao, W. Lee, Y. Dai, W. Chung, J. Hung, P. Huang, W. Lin, C. Chen, $BiOxCl_y/BiO_mBr_n/BiO_pI_q/GO$ quaternary composites: Syntheses and application of visible-light-driven photocatalytic activities, J. Colloid Interface Sci. 544 (2019) 25–36, https://doi.org/10.1016/j.jcis.2019.02.067.

[19] C. Siao, H. Chen, L. Chen, J. Chang, T. Yeh, C. Chen, Controlled hydrothermal synthesis of bismuth oxychloride/bismuth oxybromide/bismuth oxyiodide composites exhibiting visible-light photocatalytic degradation of 2-hydroxybenzoic acid and crystal violet, J. Colloid Interface Sci. 526 (2018) 322–336, https://doi.org/10.1016/j.jcis.2018.04.097.

[20] J. Li, Y. Yu, L. Zhang, Bismuth oxyhalide nanomaterials: layered structures meet photocatalysis, Nanoscale 6 (2014) 8473–8488, https://doi.org/10.1039/C4NR02553A.

[21] J. Di, J. Xia, Y. Ge, L. Xu, H. Xu, M. He, Q. Zhang, H. Li, Reactable ionic liquid-assisted rapid synthesis of BiOI hollow microspheres at room temperature with enhanced photocatalytic activity, J. Mater. Chem. A 2 (2014) 15864–15874, https://doi.org/10.1039/C4TA02400A.

[22] J. Zhang, X. Chen, K. Takanabe, K. Maeda, K. Domen, J.D. Epping, X. Fu, M. Antonietti, X. Wang, Synthesis of a carbon nitride structure for visible-light catalysis by copolymerization, Angew. Chem. Int. Ed. 49 (2010) 441–444, https://doi.org/10.1002/anie.200903886.

[23] A. Meng, W. Tian, H. Yang, X. Wang, X. Wang, Z. Li, Molybdenum sulfide-modified metal-free graphitic carbon nitride/black phosphorus photocatalyst synthesized via high-energy ball-milling for efficient hydrogen evolution and hexavalent chromium reduction, J. Hazard. Mater. 413 (2021), 125400, https://doi.org/10.1016/j.jhazmat.2021.125400.

[24] Q. Wang, J. Lian, J. Li, R. Wang, H. Huang, B. Su, Z. Lei, Highly efficient photocatalytic hydrogen production of flower-like cadmium sulfide decorated by histidine, Sci. Rep. 5 (2015) 13593, https://doi.org/10.1038/srep13593.

[25] F. Wu, F. Chang, J. Zheng, M. Jiao, B. Deng, X. Hu, X. Liu, Synthesis and photocatalytic performance of $Bi_{12}O_{17}Cl_2$ semiconductors calcined at different temperatures, J. Inorg. Organomet. Polym. Mater. 28 (2018) 721–730, https://doi.org/10.1007/s10904-017-0731-5.

[26] L. Zhang, X. Yue, J. Liu, J. Feng, X. Zhang, C. Zhang, R. Lia, C. Fan, Facile synthesis of $Bi_5O_7Br/BiOBr$ 2D/3D heterojunction as efficient visible-light-driven photocatalyst for pharmaceutical organic degradation, Sep. Purif. Technol. 231 (2020), 115917, https://doi.org/10.1016/j.seppur.2019.115917.

[27] X. Gao, K. Gao, F. Fu, C. Liang, Q. Li, J. Liu, L. Gao, Y. Zhu, Synergistic introducing of oxygen vacancies and hybrid of organic semiconductor: realizing deep structure modulation on Bi_5O7I for high-efficiency photocatalytic pollutant oxidation, Appl. Catal. B 265 (2020), 118562, https://doi.org/10.1016/j.apcatb.2019.118562.

[28] B. Yang, P. Yang, L. Wang, B. Yang, H. Xie, Y. Zhou, L. Ye, Ultrathin $Bi_4O_5Br_2$ nanosheets for selective photocatalytic CO_2 conversion into CO, Chem. Eng. J. 360 (2019) 473–482, https://doi.org/10.1016/j.cej.2018.12.008.

[29] M.A.L.R.M. Cortes, J.W.J. Hamilton, P.K. Sharma, A. Brown, M. Nolan, K.A. Gray, J.A. Byrne, Formal quantum efficiencies for the photocatalytic reduction of CO_2 in a gas phase batch reactor, Catal. Today 326 (2019) 75–81, https://doi.org/10.1016/j.cattod.2018.10.047.

[30] A. Chatzitakis, C. Berberidou, I. Paspaltsis, G. Kyriakou, T. Sklaviadis, I. Poulios, Photocatalytic degradation and drug activity reduction of chloramphenicol, Water Res. 42 (2008) 386–394, https://doi.org/10.1016/j.watres.2007.07.030.

[31] H. Chen, F. Liu, X. Xiao, J. Hu, B. Gao, D. Zou, C. Chen, Visible-light-driven photocatalysis of carbon dioxide and organic pollutants by $MFeO_2$ (M = Li, Na, or K), J. Colloid Interface Sci. 601 (2021) 758–772, https://doi.org/10.1016/j.jcis.2021.05.156.

[32] F. Liu, Y. Dai, F. Chen, C. Chen, Lead bismuth oxybromide/graphene oxide: synthesis, characterization, and photocatalytic activity for removal of carbon dioxide, crystal violet dye, and 2-hydroxybenzoic acid, J. Colloid Interface Sci. 562 (2020) 112–124, https://doi.org/10.1016/j.jcis.2019.12.006.

[33] L. Hao, H. Huang, Y. Guo, Y. Zhang, Multifunctional $Bi_2O_2(OH)(NO_3)$ nanosheets with {001} active exposing facets: efficient photocatalysis, dye-sensitization, and piezoelectric-catalysis, ACS Sustain. Chem. Eng. 6 (2018) 1848–1862, https://doi.org/10.1021/acssuschemeng.7b03223.

[34] W. Ma, N. Wang, Y. Fan, T. Tong, X. Han, Y. Du, Non-radical-dominated catalytic degradation of bisphenol a by ZIF-67 derived nitrogen-doped carbon nanotubes frameworks in the presence of peroxymonosulfate, Chem. Eng. J. 336 (2018) 721–731, https://doi.org/10.1016/j.cej.2017.11.164.